

Searching for Axion-like particle Dark Matter with Time-domain Polarization: Constraints from a protoplanetary disk

Kanako Narita

Department of Astronomy, Graduate School of Science,

The University of Tokyo, 7-3-1 Hongo,

Bunkyo-ku, Tokyo 113-0033, Japan and

Also at Department of Astronomy, Graduate School of Science,

The University of Tokyo, Tokyo 113-0033, Japan

Tomohiro Fujita

Department of Physics, Ochanomizu University,

2-1-1 Otsuka, Bunkyo-ku, Tokyo 112-8610, Japan and

Kavli Institute for the Physics and Mathematics of the Universe (WPI),

The University of Tokyo Institutes for Advanced Study,

The University of Tokyo, Chiba 277-8583, Japan

Ryo Tazaki

Department of Earth Science and Astronomy,

Graduate School of Arts and Sciences,

The University of Tokyo, 3-8-1 Komaba,

Meguro-ku, Tokyo 153-8902, Japan

Bunyo Hatsukade

National Astronomical Observatory of Japan,

2-21-1 Osawa, Mitaka, Tokyo 181-8588, Japan

Graduate University for Advanced Studies, SOKENDAI,

Osawa, Mitaka, Tokyo 181-8588, Japan and

Department of Astronomy, Graduate School of Science,

The University of Tokyo, 7-3-1 Hongo,

Bunkyo-ku, Tokyo 133-0033, Japan

(Dated: February 18, 2026)

Abstract

Axion-like particles (ALPs) can induce a birefringence effect that rotates the polarization angle of light, offering a probe of ultralight dark matter. We analyze archival near-infrared polarimetric data of the protoplanetary disk (PPD) around HD 163296. Whereas previous studies considered only single-epoch snapshots, we perform a consistent multi-epoch time-series analysis, extracting the polarization angle and its uncertainty from the polarized images. The resulting six-epoch time series is consistent with a constant polarization angle within the measurement uncertainties, while being sensitive to timescales of \sim 170–400 days. The typical polarization angle uncertainties are 1.6° – 6.4° , and are partly driven by multiple scattering in the optically thick disk, which broadens the intrinsic polarization angle distribution and introduces additional dispersion in the representative polarization angle. Based on these data, we derive the first upper limits on the ALP–photon coupling from PPD polarization variability, $g_{a\gamma} \lesssim 7.5 \times 10^{-12} (m_a/10^{-22} \text{ eV}) \text{ GeV}^{-1}$. Furthermore, we forecast that achieving a polarization angle uncertainty of $\sigma_\chi \sim 0.1^\circ$ would enable world-leading sensitivity to ALP-induced birefringence.

I. INTRODUCTION

The identification of the nature of dark matter has remained a key open problem in both physics and astronomy for decades. While the cold dark matter (CDM) paradigm successfully reproduces the large-scale structure of the Universe, it faces several tensions with observations on galactic scales, such as the core–cusp problem [1]. As a potential resolution to these discrepancies, dark matter with an extremely small mass ($m \sim 10^{-22} \text{ eV}$) has attracted considerable attention [2, 3]. At such ultralight masses, quantum mechanical effects become significant even on astrophysical scales, leading to the suppression of structure formation on small scales.

Among the many dark matter candidates, axion-like particles (ALPs) are a particularly promising option to account for these discrepancies. ALPs are pseudo-scalar fields that couple to photons via a Chern–Simons term. The original axion was introduced as a pseudo-Nambu–Goldstone boson associated with the Peccei–Quinn mechanism to solve the strong CP problem in quantum chromodynamics (QCD) [4–7], and ALPs are also predicted by string theories [8–10]. Unlike the QCD axion, the mass and coupling constants of ALPs are not necessarily related, allowing for a wide range of phenomenological possibilities. In par-

ticular, ALPs with extremely small masses ($m \sim 10^{-22}$ eV) can behave as ultralight bosonic fields and constitute so-called fuzzy dark matter, which suppresses small-scale structure formation through quantum pressure effects [2, 11]. This scenario not only provides a viable dark matter candidate, but also offers a natural resolution to the small-scale problems inherent in the standard CDM framework. Here, we assume that dark matter, including ALPs, is of the Axion Dark Matter (ADM) type.

ADM has been searched for across a broad mass range using a variety of optical and astrophysical approaches, yet there remain mass ranges where current methods have limited sensitivity. Two main observational strategies have been employed to search for ADM. The first is the conversion between axions and photons in the presence of magnetic fields, which has been exploited in laboratory experiments such as axion helioscopes [12, 13] and light-shining-through-a-wall setups [14]. Astrophysical observations, including studies of SN1987A [15] and distant quasars [16], have also been used to search for signatures of this conversion. To date, no definitive signal has been detected (though see Refs. [17–19] for tentative hints). Because the conversion probability depends on the coupling constant $g_{a\gamma}$ and on the strength and morphology of intervening magnetic fields, these astrophysical constraints typically set upper limits of $g_{a\gamma} \lesssim 10^{-11}$ GeV $^{-1}$ for $m \lesssim 10^{-14}$ eV, but remain subject to uncertainties in cosmic magnetic field properties.

The second approach is to search for photon birefringence induced by an axion background [20, 21]. If ADM exists, its coupling to photons can lead to a rotation of the polarization angle of light, depending on the variation of the ALP field between the emission and detection points (see Section II for details). In previous applications, this method has been applied to polarization maps of the cosmic microwave background (CMB), where the birefringence induced by axion-like or axion dark matter is probed through map-based statistical analyses rather than time-domain measurements. In particular, the spatial power spectrum of the polarization rotation angle and its impact on the CMB polarization power spectra, including the depolarization (washout) of the primordial E modes, are evaluated and compared with observations to constrain the ADM–photon coupling and the particle mass [22]. While the majority of previous birefringence searches have been limited to static, map-based analyses, recent efforts have extended to the time domain [e.g., 23, 24]. These studies target bright, polarized astrophysical sources such as Tau A and pulsars, aiming to detect periodic or otherwise temporally varying polarization rotations [25]. By moni-

toring these sources over extended periods, time-domain analyses have, in certain cases, exceeded the sensitivity of static approaches, with recent pulsar observations providing the most stringent constraints to date on specific regions of the ADM parameter space [26].

Protoplanetary disks (PPDs) are flattened, optically thick composed of gas and dust surrounding young stars, where planets are thought to form. The optical thickness arises primarily from dust absorption and scattering. In optical and near-infrared bands, the disk is visible in scattered stellar light by dust grains in the disk surface regions, which produces a well-understood linear polarization pattern at the source [e.g., 27]. This predictable geometry allows the observed polarization angle to serve as a sensitive probe of any rotation caused by birefringence during photon propagation. PPDs offer a large ensemble of spatially resolved, polarized sources observed over multiple epochs, providing numerous measurements of polarization angles. This makes them ideal targets for probing potential time-dependent birefringence effects predicted by ADM–photon interactions, while also enhancing the statistical sensitivity of such searches [28]. Using this method, a study analyzing snapshot polarization images of PPDs has placed a constraint on the coupling constant of $g_{a\gamma} < 5 \times 10^{-13} \left(\frac{m}{10^{-22} \text{ eV}} \right) \text{ GeV}^{-1}$ [29]. However, in reality protoplanetary disks often deviate from strict axisymmetry: planet formation, magnetic fields, spiral density waves, and gravitational instabilities can all introduce intrinsic departures from centrosymmetric polarization pattern [e.g., 27]. While such effects do not necessarily invalidate snapshot-based polarization analyses—particularly when deriving conservative constraints, they indicate that care must be taken when discussing the detection of temporal variations under an axisymmetric assumption [29].

In this work, we instead adopt a time-series approach, focusing on relative temporal variations in the polarization angle. Because this method relies on changes within the same system rather than on the absolute polarization pattern, it remains robust even when the disk exhibits intrinsic asymmetries. This provides a key advantage: time-domain analysis enables an axion search that is less sensitive to the detailed astrophysical morphology of individual PPDs.

The structure of this paper is as follows. Section I introduces the scientific background and motivation, emphasizing the potential of PPDs for probing ultralight axion-like dark matter. Section II summarizes the theoretical framework for ALP-induced polarization rotation. Section III explains the methodology for estimating polarization angles and their

uncertainties from the polarization maps, as well as for deriving upper limits on the coupling constant. Section IV presents the results of our analysis, including the constraints on the axion–photon coupling from a PPD around HD 163296 and forecasts for achievable polarization angle precision. Section V discusses observational prospects, limitations of joint analyses, and potential systematic effects. Finally, Section VI summarizes our findings and outlines future directions.

II. THEORETICAL FRAMEWORK OF ADM-INDUCED POLARIZATION ROTATION

In this section, we outline the theoretical framework of ADM-induced polarization rotation. The rotation angle of the photon polarization plane is proportional to the difference in the ALP field values between the source at the emission time $(t_{\text{emit}}, \mathbf{x}_{\text{emit}})$ and the observer at the observation time $(t_{\text{obs}}, \mathbf{x}_{\text{obs}})$ [29]:

$$\chi(t_{\text{obs}}, x_{\text{obs}}, t_{\text{emit}}, x_{\text{emit}}) = -\frac{g_{a\gamma}}{2} [\phi(t_{\text{obs}}, \mathbf{x}_{\text{obs}}) - \phi(t_{\text{emit}}, \mathbf{x}_{\text{emit}})], \quad (1)$$

where $g_{a\gamma}$ is the ADM–photon coupling constant. The local ADM field in our Milky Way Galaxy can be approximated by [30]

$$\phi(t, \mathbf{x}) = \phi_0 \cos(m_a t + \delta(\mathbf{x})), \quad (2)$$

where ϕ_0 is the averaged amplitude, $\delta(\mathbf{x})$ is the phase depending on the position, and m_a is the ADM mass. Substituting this into Equation (1) and rearranging, we obtain

$$\chi = g_{a\gamma} \phi_0 \sin \Xi \sin(m_a t_{\text{obs}} + \Xi + \delta_{\text{emit}}), \quad (3)$$

where $\Xi \equiv \frac{1}{2} [m_a(t_{\text{obs}} - t_{\text{emit}}) + \delta_{\text{obs}} - \delta_{\text{emit}}]$ is constant because $t_{\text{obs}} - t_{\text{emit}} = \frac{d}{c}$, which corresponds to the fixed light-travel time from the source to the observer, with d being the source–observer distance. In this form, the rotation angle is expressed as a time oscillation with a coefficient of $\sin \Xi$. From the local dark matter density, $\rho_{\text{DM}} \simeq 0.3 \text{ GeV cm}^{-3}$ [31], the amplitude can be estimated as $\phi_0^2 \simeq 2\rho_{\text{DM}}/m_a^2$. For convenience, we define

$$g_{12} \equiv \frac{g_{a\gamma}}{10^{-12} \text{ GeV}^{-1}}, \quad m_{22} \equiv \frac{m_a}{10^{-22} \text{ eV}}.$$

The rotation angle can then be written as

$$\chi(t, T) \approx 2 \times 10^{-2} \sin \Xi \sin(m_a t_{\text{obs}} + \Xi + \delta_{\text{emit}}) g_{12} m_{22}^{-1}. \quad (4)$$

In practical observations, Ξ is dominated by the term $m_a(t_{\text{obs}} - t_{\text{emit}})$, which becomes much greater than unity for the ALP masses considered here. Because $\Xi \gg 1$, the phase is effectively randomized, and $\sin \Xi$ can be approximated as a random variable with mean zero and rms $1/\sqrt{2}$. Applying this to the amplitude yields

$$\chi(t_{\text{obs}}, T) \simeq 1.4 \times 10^{-2} \sin(m_a t_{\text{obs}} + \text{const.}) g_{12} m_{22}^{-1}, \quad (5)$$

indicating that the polarization angle exhibits a sinusoidal time variation with angular frequency $\omega = m_a$, and that the effective amplitude is proportional to $g_{a\gamma}/m_a$. In previous work based on single-epoch (snapshot) polarization images of PPDs [29], the time-dependent factor $\sin(m_a t + \text{const})$ could not be observationally resolved, because snapshot images do not provide temporal sampling of the modulation. As a result, the amplitude could only be estimated by adopting its rms expectation value of $1/\sqrt{2}$. In contrast, the multi-epoch observations used in this study allow us to sample the temporal evolution predicted by (5) and to search directly for the sinusoidal modulation without relying on this rms-based approximation. This represents a key methodological improvement over previous snapshot-based analyses. In the context of PPDs, the intrinsic polarization geometry is well understood: scattered light from submicron-sized dust grains on the disk surface produces polarization vectors that are nearly azimuthal, i.e., perpendicular to the radial direction from the central star [e.g., 32]. This provides a well-defined reference orientation for the polarization angle at each epoch. Thus, since axion-induced polarization rotation arises as a propagation effect, it is expected to act uniformly across the disk rather than producing spatially varying deviations from the azimuthal pattern. In this work, we thus focus on the disk-integrated polarization angle by computing an inverse-variance weighted mean angle for each epoch, and search for temporal variations in this spatially averaged quantity, as would be induced by an axion-like field according to Equation (5). Figure 1 illustrates this concept, where the scattered light from the disk surface produces azimuthal polarization vectors, and a small additional rotation χ represents the possible birefringence signal to be searched for.

III. METHODS

This section details our approach for estimating polarization angles and their measurement uncertainties, followed by the framework used to compute upper limits on temporal

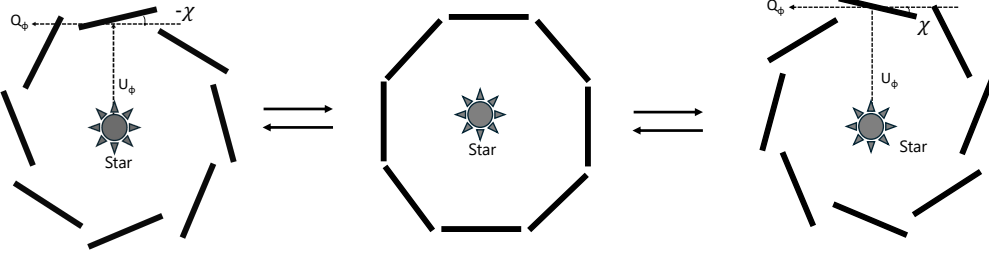


FIG. 1. Schematic illustration of the polarization geometry in a protoplanetary disk (PPD) and the expected effect of ALP-induced birefringence. The central panel shows the intrinsic azimuthal polarization pattern produced by scattered light on the disk surface. Polarization is analyzed using local Stokes parameters Q_ϕ and U_ϕ defined in the azimuthal frame; the left and right panels illustrate the corresponding polarization orientations. In the presence of ALP birefringence, the polarization plane is rotated by an angle χ , which oscillates in time, producing a time-varying polarization angle as described by Equation 5.

polarization rotation in the presence of axion-like dark matter.

A. Estimation of polarization angles and uncertainties

We first derive the azimuthal Stokes parameters Q_ϕ and U_ϕ by rotating the linear Stokes parameters Q and U into a polar coordinate frame centered on the star [33, 34]:

$$\begin{aligned} Q_\phi &= -Q \cos(2\phi) - U \sin(2\phi), \\ U_\phi &= Q \sin(2\phi) - U \cos(2\phi), \end{aligned} \quad (6)$$

where ϕ is the position angle of each pixel measured from north through east. In this convention, $Q_\phi > 0$ corresponds to an azimuthal (tangential) polarization pattern, while U_ϕ represents deviations from perfect azimuthal symmetry. We then construct polarized intensity maps as

$$P = \sqrt{Q_\phi^2 + U_\phi^2}. \quad (7)$$

The noise level σ is estimated from emission-free regions of the U_ϕ map. Pixels satisfying $R > 5\sigma$ are retained and grouped into 3×3 pixel blocks, each corresponding to one independent beam. A circular region of radius 22 pixels centered on the stellar position is additionally masked to remove the central area strongly affected by stellar emission. In addition, to confine the analysis to the observed extent of the scattered-light disk and suppress

spurious high-significance features near the edge of the field, all pixels at projected radii exceeding $r_{\text{out}} = 70$ pixels from the stellar position are excluded. The adopted value of r_{out} encompasses the full bright scattering ring in all epochs while avoiding isolated background fluctuations. We have verified that moderate variations of r_{out} within a reasonable range do not qualitatively affect the derived upper limits.

For each block $b = 1, \dots, N_{\text{block}}$, corresponding to an individual 3×3 pixel block, let its valid pixels be indexed by $i = 1, \dots, N_{\text{pix},b}$. Here, the index b labels individual 3×3 blocks, and $N_{\text{pix},b}$ denotes the number of finite pixels within each block, which may vary due to masking and data selection. The block-averaged Stokes parameters are

$$\bar{Q}_{\phi,b} = \frac{1}{N_{\text{pix},b}} \sum_{i=1}^{N_{\text{pix},b}} Q_{\phi,i}, \quad \bar{U}_{\phi,b} = \frac{1}{N_{\text{pix},b}} \sum_{i=1}^{N_{\text{pix},b}} U_{\phi,i}. \quad (8)$$

Assuming a uniform rms noise (σ_Q, σ_U) across the image, the uncertainties of the block-averaged Stokes parameters follow from standard variance propagation:

$$\sigma_{\bar{Q},b}^2 = \frac{\sigma_Q^2}{N_{\text{pix},b}}, \quad \sigma_{\bar{U},b}^2 = \frac{\sigma_U^2}{N_{\text{pix},b}}. \quad (9)$$

From these block-averaged values, the polarization angle was computed as

$$\chi_b = \frac{1}{2} \arctan \left(\frac{\bar{U}_{\phi,b}}{\bar{Q}_{\phi,b}} \right). \quad (10)$$

which follows from the standard definition of the polarization angle.

The uncertainty of χ was obtained via linear error propagation. For a function

$$\chi_b = f(\bar{Q}_{\phi,b}, \bar{U}_{\phi,b}), \quad (11)$$

the variance is given by

$$\sigma_{\chi,b}^2 = \left(\frac{\partial f}{\partial \bar{Q}_{\phi,b}} \right)^2 \sigma_{\bar{Q},b}^2 + \left(\frac{\partial f}{\partial \bar{U}_{\phi,b}} \right)^2 \sigma_{\bar{U},b}^2, \quad (12)$$

where we have assumed that the uncertainties in \bar{Q}_{ϕ} and \bar{U}_{ϕ} are uncorrelated.

The required partial derivatives are

$$\frac{\partial \chi_b}{\partial \bar{Q}_{\phi,b}} = -\frac{1}{2} \frac{\bar{U}_{\phi,b}}{\bar{Q}_{\phi,b}^2 + \bar{U}_{\phi,b}^2}, \quad \frac{\partial \chi_b}{\partial \bar{U}_{\phi,b}} = \frac{1}{2} \frac{\bar{Q}_{\phi,b}}{\bar{Q}_{\phi,b}^2 + \bar{U}_{\phi,b}^2}, \quad (13)$$

which, inserted into Equation (12), give

$$\sigma_{\chi,b}^2 = \left[-\frac{1}{2} \frac{\bar{U}_{\phi,b}}{\bar{Q}_{\phi,b}^2 + \bar{U}_{\phi,b}^2} \right]^2 \sigma_{\bar{Q},b}^2 + \left[\frac{1}{2} \frac{\bar{Q}_{\phi,b}}{\bar{Q}_{\phi,b}^2 + \bar{U}_{\phi,b}^2} \right]^2 \sigma_{\bar{U},b}^2 \quad (14)$$

$$= \frac{1}{4} \frac{\bar{Q}_{\phi,b}^2 \sigma_{\bar{U},b}^2 + \bar{U}_{\phi,b}^2 \sigma_{\bar{Q},b}^2}{(\bar{Q}_{\phi,b}^2 + \bar{U}_{\phi,b}^2)^2}. \quad (15)$$

Taking the square root, the uncertainty of the polarization angle becomes

$$\sigma_{\chi,b} = \frac{1}{2} \sqrt{\frac{\bar{Q}_{\phi,b}^2 \sigma_{\bar{U},b}^2 + \bar{U}_{\phi,b}^2 \sigma_{\bar{Q},b}^2}{\bar{Q}_{\phi,b}^2 + \bar{U}_{\phi,b}^2}}. \quad (16)$$

This block-averaging procedure effectively reduces pixel-pixel correlations by treating each 3×3 pixels region as one independent beam, thereby providing a more stable estimate of the per-epoch polarization angle and its statistical uncertainty.

After computing the polarization angles and their uncertainties for all independent blocks, we derived the disk-integrated polarization angle for each epoch. In studies of interstellar polarization, the measurement uncertainties are often relatively homogeneous across sight lines, and therefore polarization angles are frequently averaged without applying explicit statistical weighting [e.g., 35]. However, Appendix C of Doi *et al.* [35] demonstrates that axial (180°-periodic) angles can be combined within the framework of circular statistics by assigning each doubled-angle vector a length proportional to a chosen weight. In our application, where the per-block uncertainties vary substantially across the disk, such a weighted formulation is essential. We therefore adopt this generalized approach by letting each block contribute a doubled-angle vector whose length is given by the inverse-variance weight $w_b = 1/\sigma_{\chi,b}^2$. This provides a statistically consistent extension of standard circular averaging and leads naturally to the weighted axial mean described below. Because the polarization angle is an axial (180°-periodic) quantity, the averaging must be performed in the doubled-angle space (2θ) [36]. The weighted mean angle is therefore

$$\bar{\chi} = \frac{1}{2} \arctan 2 \left(\sum_b w_b \sin 2\chi_b, \sum_b w_b \cos 2\chi_b \right), \quad (17)$$

where $w_b = 1/\sigma_{\chi,b}^2$ are inverse-variance weights.

Here, $\arctan 2(y, x)$ denotes the quadrant-preserving inverse tangent, defined by

$$\arctan 2(y, x) = \begin{cases} \arctan\left(\frac{y}{x}\right), & x > 0, \\ \arctan\left(\frac{y}{x}\right) + \pi, & x < 0, y \geq 0, \\ \arctan\left(\frac{y}{x}\right) - \pi, & x < 0, y < 0, \\ +\frac{\pi}{2}, & x = 0, y > 0, \\ -\frac{\pi}{2}, & x = 0, y < 0, \\ \text{undefined,} & x = 0, y = 0. \end{cases} \quad (18)$$

Unlike the conventional $\arctan(y/x)$, which is restricted to the range $(-\pi/2, \pi/2)$ and therefore loses quadrant information, $\arctan 2(y, x)$ returns an angle in the full range $(-\pi, \pi]$, ensuring that the correct angular branch is used when averaging axial (180°-periodic) quantities such as the polarization angle.

The standard deviation of the resulting distribution of representative polarization angles is adopted as the uncertainty. In practice, it is computed as [36]

$$\sigma_{\text{axial}} = \frac{1}{2} \sqrt{-2 \ln R}, \quad R = \frac{\sqrt{(\sum_b w_b \cos 2\chi_b)^2 + (\sum_b w_b \sin 2\chi_b)^2}}{\sum_b w_b}. \quad (19)$$

This procedure correctly accounts for both the angular periodicity of the polarization angle and the spatially varying uncertainties across the disk, providing a statistically robust estimate of the epoch-averaged polarization angle and its corresponding uncertainty.

B. Estimation of upper limits

To constrain possible polarization-angle modulations induced by ALPs, we quantify the maximum sinusoidal amplitude consistent with the data. Because the number of epochs is limited in the dataset used in this study, a full periodic search (e.g., least-squares spectral analysis) is not statistically meaningful. Instead, we derive frequentist upper limits based on Monte Carlo (MC) simulations that faithfully reproduce the actual sampling cadence and measurement uncertainties.

For each target, we first construct the polarization angle time series $\{\chi_i\}$ and corresponding 1σ uncertainties $\{\sigma_i\}$, where the index i labels individual observing epochs. Under the

null hypothesis of no intrinsic polarization angle variation, we generate $N_{\text{MC}} = 10^5$ mock time series $\{\chi_i^{(k)}\}$ by drawing Gaussian noise realizations with standard deviations σ_i at the observed epochs. Each realization is fitted with a sinusoidal model,

$$\chi(t) = A \sin(2\pi ft + \phi) + \chi_0, \quad (20)$$

where A is the modulation amplitude, f is the trial frequency corresponding to an ALP mass $m_a = 2\pi f$, ϕ is the phase, and χ_0 is the mean polarization angle. We minimize the χ^2 statistic over (A, ϕ, χ_0) for each realization to obtain the best-fit amplitude $A^{(k)}$.

The resulting distribution $\{A^{(k)}\}$ represents the noise-only expectation for each frequency. From this distribution, we define the 95% confidence-level (CL) upper limit $A_{95}(f)$ by

$$\mathbb{P}(A^{(k)} < A_{95}(f)) = 0.95. \quad (21)$$

Applying the same fitting procedure to the observed data shows that all trial frequencies are consistent with the null hypothesis within the 95% CL.

To express the theoretical amplitude predicted by Equation 5 in degrees, we first note that Equation 5 gives the axion-induced polarization rotation with an amplitude in radians,

$$A_{\text{theory}}(\text{rad}) = 1.4 \times 10^{-2} g_{12} m_{22}^{-1}. \quad (22)$$

Using the standard conversion $1 \text{ rad} = 180/\pi \text{ deg}$, the corresponding amplitude in degrees becomes

$$A_{\text{theory}}(\text{deg}) = 0.80^\circ g_{12} m_{22}^{-1}. \quad (23)$$

Requiring that the observed 95% upper limit A_{95} satisfies $A_{95} \geq A_{\text{theory}}$, the axion–photon coupling is constrained as

$$g_{12} < 1.25 \left(\frac{A_{95}}{1^\circ} \right) m_{22}, \quad (\text{for } \rho_{\text{DM}} = 0.3 \text{ GeV cm}^{-3}). \quad (24)$$

IV. DATA AND RESULTS

A. Observational Data

The target of this study, the protoplanetary disk around HD 163296 (R.A. = 17:56:21.29, decl. = -21:57:21.87) is one of sources included in larger SPHERE/IRDIS survey of 29

TABLE I. Stellar properties and observing log of HD 163296 adopted in this work [37].

Property	Value
Associated molecular cloud	None
Distance	$101.0_{-0.4}^{+0.4}$ pc
Stellar luminosity	$15.9_{-0.3}^{+0.3} L_{\odot}$
Stellar mass	$2.0 M_{\odot}$
Age	10–12 Myr
Date (UTC)	t_{exp} (s)
2021-04-06	384
2021-06-03	2048
2021-09-09	1536
2021-09-26	512
2022-06-11	3072
2022-07-07	3072

protoplanetary disks obtained in the Ks band using the star-hopping mode [37]. The observations were carried out under six ESO programs (0103.C-0470, 105.209E, 105.20HV, 106.21HJ, 108.22EE; PI: M. Benisty, and 105.20JB; PI: M. Keppler). These data were taken in DPI mode with pupil tracking, allowing simultaneous total-intensity and polarized-light imaging. In the star-hopping strategy, each disk-hosting target is paired with a well-matched reference star to obtain quasi-simultaneous wavefront calibration, thereby improving speckle subtraction and the detection of circumstellar structures [38]. Among the survey targets, a protoplanetary disk around HD 163296 offers the richest time-domain sampling, providing six epochs suitable for our polarization angle variability analysis. The six SPHERE/IRDIS epochs used in this study were obtained on 2021 April 6, 2021 June 3, 2021 September 9, 2021 September 26, 2022 June 11, and 2022 July 7. A comprehensive description of the survey design, observing setup, and data reduction procedures is presented in [37]. The stellar properties of HD 163296 are taken from [37] and summarized in Table I.

B. The polarization angle measurements and constraints on coupling constant from the protoplanetary disk around HD 163296

Figure 2 shows the time series of the disk-averaged polarization angle for HD 163296, derived from the Q_ϕ and U_ϕ images at each epoch. Across all epochs, the representative polarization angles are mutually consistent within the measurement uncertainties, and no statistically significant temporal variability is detected. The observed scatter in the polarization angle measurements can be fully accounted for by the estimated uncertainties. As a result, the present data provide no evidence for polarization-angle variations arising from exotic physics such as axion-induced birefringence. Probing subtler temporal variations or coherent periodic signals will require observations with higher cadence and a longer temporal baseline than available in the current dataset. In addition, combining polarization time-series observations of multiple sources spanning different physical environments will be essential to distinguish propagation effects, such as axion-induced polarization rotation, from source-intrinsic astrophysical variability. Using this polarization angle time series, we demonstrate the feasibility of constraining ALP-induced birefringence with PPDs. Although the number of epochs is insufficient to perform a detection search, we can place a statistically meaningful 95% confidence-level upper limit on the amplitude of possible polarization-angle modulations. We applied the sinusoidal fitting and Monte Carlo procedure described in Section III to the HD 163296 polarization angle time series. The temporal sampling of this dataset spans $T_{\text{span}} \simeq 399$ days with a median interval of $\Delta t_{\text{med}} \simeq 49$ days, providing sensitivity to oscillation periods of ~ 100 –400 days. No significant periodic modulation was detected at any trial frequency. The 95% confidence-level upper limits on the modulation amplitude, $A_{95}(f)$, are translated into constraints on the axion–photon coupling via Equation 24, producing the exclusion curve shown in Figure 3. Adopting the most conservative limit, $A_{95} = 6^\circ$, we obtain

$$g_{a\gamma} \lesssim 7.5 \times 10^{-12} (m_a/10^{-22} \text{ eV}) \text{ GeV}^{-1}. \quad (25)$$

We note that polarization-angle constraints derived from PPD observations can depend on how the representative angle and its uncertainty are defined. For an approximately axisymmetric disk, the central fitted value of the polarization-angle distribution is primarily determined by the geometric symmetry of the system and is therefore expected to be largely

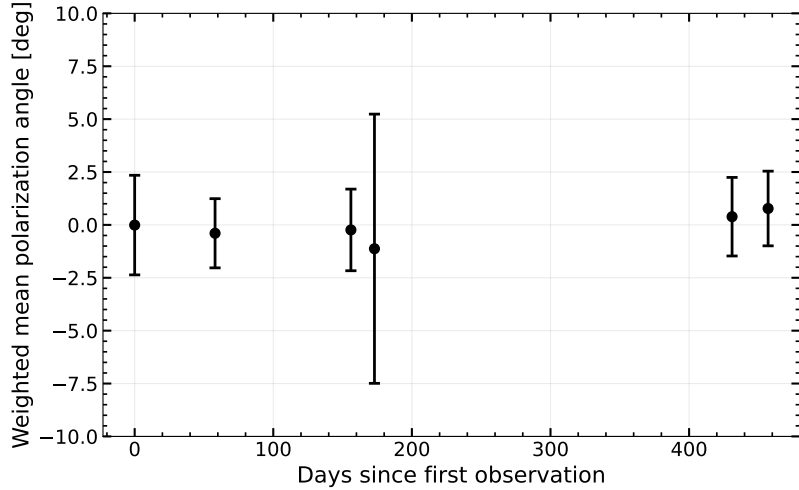


FIG. 2. The mean value of the polarization angle of HD 163296 as a function of days since 2021 April 6. Error bars represent the 1σ statistical uncertainties derived from the Stokes Q_ϕ and U_ϕ maps.

insensitive to multiple-scattering effects. In contrast, the dispersion of the polarization-angle distribution can be broadened by radiative-transfer complexities and multiple scattering within the disk atmosphere. In the previous analysis of PPD polarization [29], the bound derived from the fitted central value of the polarization angle was interpreted as an optimistic limit, while the constraint obtained from the distribution width was regarded as a conservative bound. In the present work, the statistical uncertainty of the polarization angle is evaluated directly from the observed dispersion of the angle distribution. The resulting limit is therefore directly comparable to the conservative bound. We find that our constraint is broadly consistent with the conservative limit reported in the previous study, indicating that our result is not artificially tightened by idealized assumptions and remains robust against plausible disk-scattering effects.

C. Forecast for achievable polarization angle precision

Based on the formalism introduced in Section II, the uncertainty of the polarization angle follows Equation (16), which is valid for arbitrary σ_{Q_ϕ} and σ_{U_ϕ} . In the case of $\sigma_{Q_\phi} = \sigma_{U_\phi} \equiv \sigma$, it reduces to

$$\sigma_x \approx \frac{1}{2} \frac{\sigma}{P}. \quad (26)$$

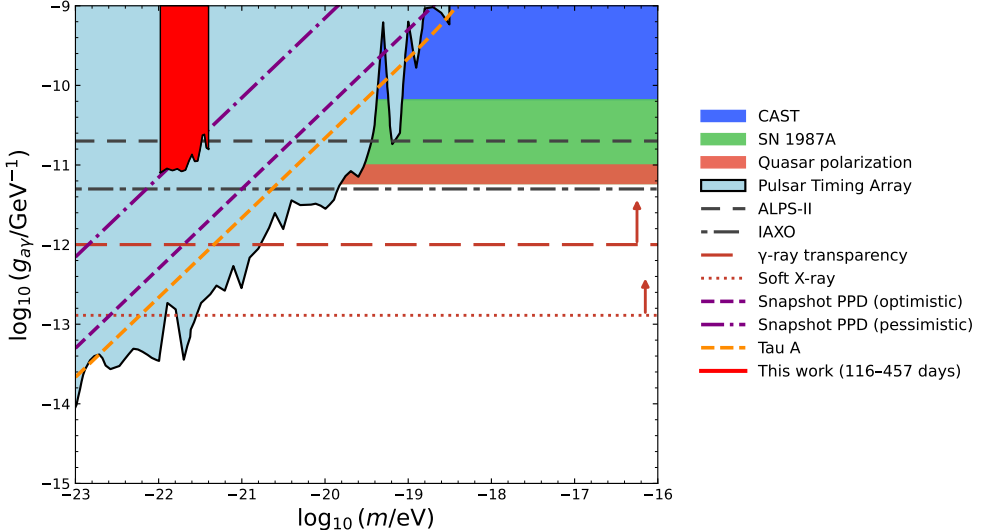


FIG. 3. 95% CL upper limit on the axion–photon coupling constant derived from the HD 163296 dataset. The accessible frequency range corresponds to oscillation periods between ~ 100 and 400 days, or ALP masses $m_a \sim 10^{-22}$ – 10^{-21} eV. The purple dash-dotted line and dashed line denote the optimistic and conservative upper bounds from PPD polarization reported by [29], respectively. The blue, green, red and light blue shaded regions are excluded by laboratory (CAST [12]) and astrophysical observations (SN 1987A [15], quasar polarization [16] and Pulsar Timing Array [26]). The black dashed lines indicate the projected sensitivities of forthcoming experiments (ALPS-II [39] and IAXO [13]), while the brown long-dashed and dotted lines represent tentative lower limits inferred from astrophysical observations (soft X-ray excess [17] and γ -ray transparency [18]).

where P is the polarized intensity defined in Equation (7), and σ denotes the rms noise of the Stokes Q_ϕ and U_ϕ maps. For a given target, if N independent pixels are available, the statistical uncertainty improves as

$$\sigma_\chi(N) \approx \frac{1}{2} \frac{1}{(R/\sigma)\sqrt{N}} = \frac{1}{2\text{SNR}\sqrt{N}}, \quad (27)$$

where $\text{SNR} \equiv R/\sigma$ represents the signal-to-noise ratio per pixel. Here, N denotes the number of statistically independent pixels contributing to the measurement. In the forecast, we assume an idealized situation in which all contributing pixels have comparable signal-to-noise ratios and probe the same underlying polarization signal. Equation (27) allows us to forecast the observational requirements to achieve a given polarization angle precision.

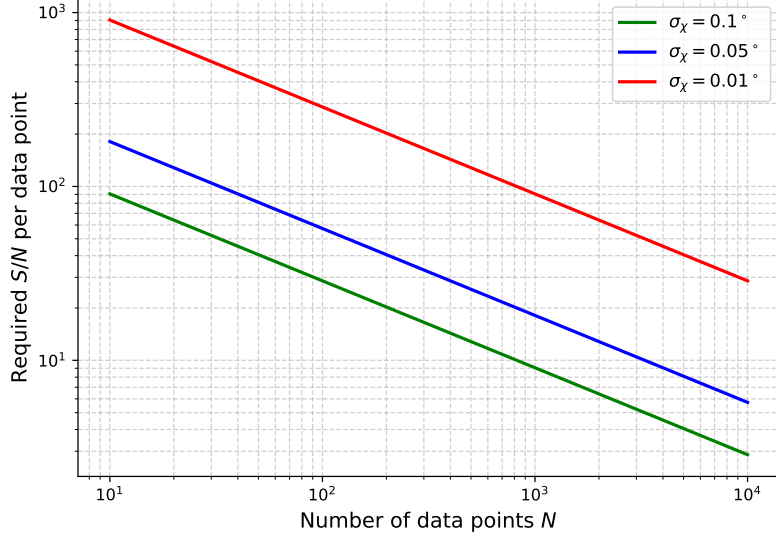


FIG. 4. Required signal-to-noise ratio per measurement (S/N) as a function of the number of independent data points N to achieve different target precisions in the polarization angle: $\sigma_\chi = 0.1^\circ$ (green), 0.01° (red) and 0.05° (blue). The shaded regions indicate the parameter space where the corresponding precision is attainable. The figure illustrates the trade-off between observational depth (S/N) and cadence (N), and shows that sub-degree to sub-millidegree polarization angle precision is feasible with a sufficiently large number of high-quality observations.

Specifically, the condition can be written as

$$\text{SNR}\sqrt{N} \gtrsim \frac{1}{2\sigma_\chi}. \quad (28)$$

For a target precision of $\sigma_\chi = 0.01^\circ$, this requires $\text{SNR}\sqrt{N} \gtrsim 5700$.

These scaling relations are illustrated in Fig. 4, where the required signal-to-noise ratio per pixel is shown as a function of the number of independent pixels N for different target precisions. The figure highlights the trade-off between observational depth (SNR per pixel) and spatial sampling (N), and demonstrates that sub-degree to sub-millidegree polarization angle precision is, in principle, achievable given sufficient data quality and cadence.

Here we aimed to obtain a statistically reliable estimate of the upper limit on the polarization angle modulation amplitude A_{lim} under a setup that closely reflects actual observations. Specifically, we assumed a realistic monitoring campaign in which a representative target in Taurus can be observed for ~ 150 nights per year, and extended this cadence over a 10-year period. Using the achievable values of $\sigma_\chi(N)$ for such a single target, we generated noise-

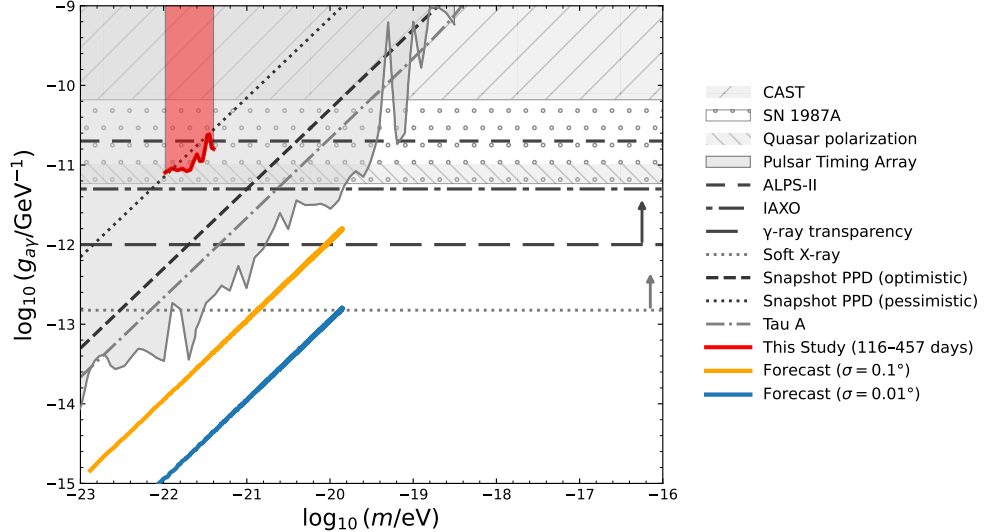


FIG. 5. Forecasted 95% confidence-level (CL) sensitivities on the axion–photon coupling $g_{a\gamma}$ achievable with long-term monitoring of protoplanetary disks. The orange and blue dotted lines correspond to expected limits for polarization angle precisions of 0.1° and 0.01° , respectively. Other shaded regions and reference limits are the same as in Fig 3.

only time-series realizations matched to this cadence. Through this procedure, we evaluated the expected distribution of fitted amplitudes and hence the corresponding sensitivity to the ALP–photon coupling constant.

This projected limit is stronger than existing astrophysical bounds and highlights the potential of multi-epoch PPD observations as an independent probe of ultralight axion-like dark matter.

V. DISCUSSION

A. Outlook

In this study, we focus on optically thick PPDs, in which multiple scattering by dust grains plays a crucial role. As a result of this multiple scattering, the spatial distribution of polarization angles is broadened to scales of several tens of degrees, and an intrinsic uncertainty at the level of a few degrees is introduced in the determination of the representative polarization angle. In contrast, for optically thin debris disks [e.g., 40], where no additional physical mechanisms break axisymmetry, multiple scattering is expected to be negligible

and single scattering dominates. Under such idealized conditions, the polarization angle distribution approaches a delta-function-like profile if we neglect instrumental errors, enabling an extremely precise determination of the intrinsic polarization angle. Debris disks therefore provide particularly clean targets for probing minute polarization rotations. However, debris disks are generally faint in scattered light, making high-precision polarimetric measurements challenging with current ground-based telescopes. In addition to target selection, the achievable polarization angle precision itself is a key factor. The attainable precision depends not only on the signal-to-noise ratio, but also strongly on the number of independent measurements N , as expressed by Equation (28). Furthermore, broader temporal sampling across multiple disks allows the search to probe a wider range of ALP masses, highlighting the importance of observing diverse targets over extended periods. Since a single target typically provides only a limited number of epochs, combining time-series data from a large number of disks offers a practical way to enhance sensitivity and extend temporal coverage. Consequently, a strategy that integrates long-term observations of many disks is expected to maximize the overall sensitivity to ALP-induced birefringence. The methodology and limitations of such joint analyses across multiple disks are discussed in detail in Section V B. Looking ahead, if high-sensitivity and highly stable space-based polarimetric observations become feasible for debris disks dominated by single scattering, polarization angle uncertainties could be reduced to the $\sim 0.1^\circ$ level. Achieving such precision would bring the sensitivity close to the forecasts presented in this work and open a new observational frontier for detecting extremely small birefringence effects.

B. Limitations of Joint Time-Series Analysis Across Multiple PPDs

A natural strategy to boost sensitivity is to combine multi-epoch polarization time series from different PPDs. However, such a joint (coherent) analysis is subject to two fundamental limitations: (i) the requirement of a common oscillation phase and field coherence, and (ii) distance-induced phase uncertainty. These two limitations are qualitatively different in nature: the former reflects an intrinsic phase freedom of the ALP field that cannot be constrained by independent observations, whereas the latter arises from geometric distance uncertainties and can, in principle, be mitigated by improved astrometric measurements.

(i) *Common oscillation phase and field coherence.* A coherent stack requires that all targets share not only the same ALP mass (and hence the same oscillation frequency $\omega = m_a$), but also a common oscillation *phase* of the ALP field. In principle, each source could have an independent emission phase δ_{emit} , which would introduce many additional free parameters in a combined fit. Since this intrinsic emission phase cannot be determined by other observations, it must be treated as a free parameter in a time-domain analysis. Importantly, within a single coherence domain of the ALP field, whose characteristic size is set by the de Broglie wavelength, the field phase can be regarded as spatially uniform:

$$\lambda_{\text{coh}} \simeq 40 \text{ pc} \left(\frac{10^{-22} \text{ eV}}{m_a} \right), \quad (29)$$

which corresponds to an oscillation period of approximately \sim year. This greatly reduces the parameter space, allowing all targets within the coherence length to be modeled with a single common phase. Objects separated by more than the coherence length should instead be analyzed independently or combined only incoherently (e.g., at the power spectrum level).

(ii) *Distance-induced phase uncertainty.* In contrast to the intrinsic emission phase discussed above, even within a shared coherence domain, accurate phase alignment requires correcting for the geometric light-travel delay between each source and the observer. This effect therefore does not represent an intrinsic free parameter of the model, but rather a source of phase uncertainty that can be reduced with sufficiently precise distance measurements.

Denoting the source distance by d with uncertainty σ_d , the relevant phase contribution is

$$\phi_d = \frac{m_a}{2} (t_{\text{obs}} - t_{\text{emit}}) = \frac{m_a d}{2c}, \quad (30)$$

with an associated uncertainty

$$\delta\phi_d = \frac{m_a}{2c} \delta d, \quad \sigma_{\phi_d} = \frac{m_a}{2c} \sigma_d. \quad (31)$$

For Gaia-like astrometric precision of $\sigma_d \sim 0.1$ pc, one finds $\sigma_{\phi_d} \simeq 0.75$ rad at $m_a = 10^{-22}$ eV, but $\sigma_{\phi_d} \simeq 7.5$ rad at $m_a = 10^{-21}$ eV, implying severe coherence loss at higher masses. A practical criterion for maintaining coherence is $\sigma_{\phi_d} \lesssim 1$ rad, i.e.,

$$\sigma_d \lesssim \frac{2c}{m_a} \simeq 0.13 \text{ pc} \left(\frac{10^{-22} \text{ eV}}{m_a} \right) = 0.13 \text{ pc } m_{22}^{-1}. \quad (32)$$

VI. CONCLUSION

We have presented the first time-domain analysis of polarization data from a protoplanetary disk to search for birefringence signatures induced by axion-like dark matter. Using archival near-infrared polarimetric observations of HD 163296, we performed a consistent multi-epoch analysis of the polarization angle, extending previous single-epoch studies to the time domain. As a result, the six-epoch polarization-angle time series shows no statistically significant variability beyond the measurement uncertainties.

From the absence of detectable variability, we derived the first constraints on the ALP-photon coupling based on PPD polarization, placing a 95% confidence-level upper limit of

$$g_{a\gamma} \lesssim 7.5 \times 10^{-12} \left(\frac{m_a}{10^{-22} \text{ eV}} \right) \text{ GeV}^{-1}. \quad (33)$$

Although this constraint is not yet competitive with the strongest existing astrophysical limits, it establishes PPD polarization variability as a viable and previously unexplored probe of ultralight ALPs.

A key limitation of the current dataset is the relatively large polarization angle uncertainty, which is partly driven by multiple scattering in the optically thick disk. This effect broadens the intrinsic polarization angle distribution and introduces additional dispersion in the representative polarization angle, limiting sensitivity to small birefringence-induced rotations. Nevertheless, our Monte Carlo forecasts demonstrate that substantial improvements are achievable with future observations. In particular, reaching a polarization angle precision of $\sigma_\chi \sim 0.1^\circ$ —potentially attainable in optically thin debris disks where single scattering dominates—would enable sensitivity to ALP-induced birefringence at a level that rivals or surpasses existing astrophysical constraints.

With a dense long-term monitoring strategy, consisting of ~ 150 observing epochs per year over a ~ 10 -year baseline, PPD and debris-disk polarization could probe ALP masses in the 10^{-23} – 10^{-20} eV range. This mass window is complementary to those targeted by pulsar timing arrays, CMB polarization, and other astrophysical and cosmological searches.

As such, time-domain polarimetry of circumstellar disks offers an independent and conceptually clean avenue for testing ultralight dark matter, grounded in well-understood polarization geometries. Future high-sensitivity, multi-epoch polarimetric observations will therefore open a promising new frontier in the search for axion-like dark matter.

ACKNOWLEDGMENTS

We thank Bin Ren for making the reduced VLT/SPHERE images of HD 163296 publicly available. We are grateful to Yuji Chinone, Yasuo Doi, Jun Hashimoto, Akimasa Kataoka and Naoya Kitade for fruitful discussions. This work was supported by JST SPRING, Grant Number JPMJSP2108 and by JSPS KAKENHI Grant Number 23K03424. RT was also supported by JSPS KAKENHI (Grant Numbers JP25K07351, JP25K01049). KN was supported by the International Graduate Program for Excellence in Earth-Space Science (IGPEES), the University of Tokyo.

- [1] D. H. Weinberg, J. S. Bullock, F. Governato, R. Kuzio de Naray, and A. H. G. Peter, *Proceedings of the National Academy of Science* **112**, 12249 (2015), arXiv:1306.0913 [astro-ph.CO].
- [2] W. Hu, R. Barkana, and A. Gruzinov, *Phys. Rev. Lett.* **85**, 1158 (2000), arXiv:astro-ph/0003365 [astro-ph].
- [3] L. Hui, J. P. Ostriker, S. Tremaine, and E. Witten, *Phys. Rev. D* **95**, 043541 (2017), arXiv:1610.08297 [astro-ph.CO].
- [4] R. D. Peccei and H. R. Quinn, *Phys. Rev. Lett.* **38**, 1440 (1977).
- [5] R. D. Peccei and H. R. Quinn, *Phys. Rev. D* **16**, 1791 (1977).
- [6] S. Weinberg, *Phys. Rev. Lett.* **40**, 223 (1978).
- [7] F. Wilczek, *Phys. Rev. Lett.* **40**, 279 (1978).
- [8] E. Witten, *Phys. Rev. D* **30**, 272 (1984).
- [9] A. Arvanitaki, S. Dimopoulos, S. Dubovsky, N. Kaloper, and J. March-Russell, *Phys. Rev. D* **81**, 123530 (2010), arXiv:0905.4720 [hep-th].
- [10] M. Cicoli, M. D. Goodsell, and A. Ringwald, *Journal of High Energy Physics* **2012**, 146 (2012), arXiv:1206.0819 [hep-th].
- [11] H.-Y. Schive, T. Chiueh, and T. Broadhurst, *Nature Physics* **10**, 496 (2014), arXiv:1406.6586 [astro-ph.GA].
- [12] CAST Collaboration, V. Anastassopoulos, S. Aune, K. Barth, A. Belov, H. Bräuninger, G. Cantatore, J. M. Carmona, J. F. Castel, S. A. Cetin, F. Christensen, J. I. Collar, T. Dafni, M. Davenport, T. A. Decker, A. Dermenev, K. Desch, C. Eleftheriadis, G. Fanourakis,

E. Ferrer-Ribas, H. Fischer, J. A. García, A. Gardikiotis, J. G. Garza, E. N. Gazis, T. Geralis, I. Giomataris, S. Gninenco, C. J. Hailey, M. D. Hasinoff, D. H. H. Hoffmann, F. J. Iguaz, I. G. Irastorza, A. Jakobsen, J. Jacoby, K. Jakovčić, J. Kaminski, M. Karuza, N. Kralj, M. Krčmar, S. Kostoglou, C. Krieger, B. Lakić, J. M. Laurent, A. Liolios, A. Ljubičić, G. Luzón, M. Maroudas, L. Miceli, S. Neff, I. Ortega, T. Papaevangelou, K. Paraschou, M. J. Pivovaroff, G. Raffelt, M. Rosu, J. Ruz, E. R. Chóliz, I. Savvidis, S. Schmidt, Y. K. Semertzidis, S. K. Solanki, L. Stewart, T. Vafeiadis, J. K. Vogel, S. C. Yıldız, and K. Zioutas, *Nature Physics* **13**, 584 (2017), [arXiv:1705.02290 \[hep-ex\]](https://arxiv.org/abs/1705.02290).

[13] E. Armengaud, F. T. Avignone, M. Betz, P. Brax, P. Brun, G. Cantatore, J. M. Carmona, G. P. Carosi, F. Caspers, S. Caspi, S. A. Cetin, D. Chelouche, F. E. Christensen, A. Dael, T. Dafni, M. Davenport, A. V. Derbin, K. Desch, A. Diago, B. Döbrich, I. Dratchnev, A. Dudarev, C. Eleftheriadis, G. Fanourakis, E. Ferrer-Ribas, J. Galán, J. A. García, J. G. Garza, T. Geralis, B. Gimeno, I. Giomataris, S. Gninenco, H. Gómez, D. González-Díaz, E. Guendelman, C. J. Hailey, T. Hiramatsu, D. H. H. Hoffmann, D. Horns, F. J. Iguaz, I. G. Irastorza, J. Isern, K. Imai, A. C. Jakobsen, J. Jaeckel, K. Jakovčić, J. Kaminski, M. Kawasaki, M. Karuza, M. Krčmar, K. Kousouris, C. Krieger, B. Lakić, O. Limousin, A. Lindner, A. Liolios, G. Luzón, S. Matsuki, V. N. Muratova, C. Nones, I. Ortega, T. Papaevangelou, M. J. Pivovaroff, G. Raffelt, J. Redondo, A. Ringwald, S. Russenschuck, J. Ruz, K. Saikawa, I. Savvidis, T. Sekiguchi, Y. K. Semertzidis, I. Shilon, P. Sikivie, H. Silva, H. ten Kate, A. Tomas, S. Troitsky, T. Vafeiadis, K. van Bibber, P. Vedrine, J. A. Villar, J. K. Vogel, L. Walckiers, A. Weltman, W. Wester, S. C. Yıldız, and K. Zioutas, *Journal of Instrumentation* **9** (5), T05002, [arXiv:1401.3233 \[physics.ins-det\]](https://arxiv.org/abs/1401.3233).

[14] K. Ehret, M. Frede, S. Ghazaryan, M. Hildebrandt, E.-A. Knabbe, D. Kracht, A. Lindner, J. List, T. Meier, N. Meyer, D. Notz, J. Redondo, A. Ringwald, G. Wiedemann, and B. Willke, *Physics Letters B* **689**, 149 (2010), [arXiv:1004.1313 \[hep-ex\]](https://arxiv.org/abs/1004.1313).

[15] A. Payez, C. Evoli, T. Fischer, M. Giannotti, A. Mirizzi, and A. Ringwald, *JCAP* **2015**, 006 (2015), [arXiv:1410.3747 \[astro-ph.HE\]](https://arxiv.org/abs/1410.3747).

[16] A. Payez, J. R. Cudell, and D. Hutsemékers, *JCAP* **2012**, 041 (2012), [arXiv:1204.6187 \[astro-ph.CO\]](https://arxiv.org/abs/1204.6187).

[17] S. Angus, J. P. Conlon, M. C. D. Marsh, A. J. Powell, and L. T. Witkowski, *JCAP* **2014**, 026 (2014), [arXiv:1312.3947 \[astro-ph.HE\]](https://arxiv.org/abs/1312.3947).

[18] M. Meyer, D. Horns, and M. Raue, *Phys. Rev. D* **87**, 035027 (2013), arXiv:1302.1208 [astro-ph.HE].

[19] K. Kohri and H. Kodama, *Phys. Rev. D* **96**, 051701 (2017), arXiv:1704.05189 [hep-ph].

[20] S. M. Carroll, G. B. Field, and R. Jackiw, *Phys. Rev. D* **41**, 1231 (1990).

[21] D. Harari and P. Sikivie, *Physics Letters B* **289**, 67 (1992).

[22] M. A. Fedderke, P. W. Graham, and S. Rajendran, *Phys. Rev. D* **100**, 015040 (2019), arXiv:1903.02666 [astro-ph.CO].

[23] M. M. Ivanov, Y. Y. Kovalev, M. L. Lister, A. G. Panin, A. B. Pushkarev, T. Savolainen, and S. V. Troitsky, *JCAP* **2019**, 059 (2019), arXiv:1811.10997 [astro-ph.CO].

[24] A. Caputo, L. Sberna, M. Frías, D. Blas, P. Pani, L. Shao, and W. Yan, *Phys. Rev. D* **100**, 063515 (2019), arXiv:1902.02695 [astro-ph.CO].

[25] S. Adachi, T. Adkins, C. Baccigalupi, Y. Chinone, K. T. Crowley, J. Errard, G. Fabbian, C. Feng, T. Fujino, M. Hasegawa, M. Hazumi, O. Jeong, D. Kaneko, B. Keating, A. Kusaka, A. T. Lee, A. I. Lonappan, Y. Minami, M. Murata, L. Piccirillo, C. L. Reichardt, P. Siritanasak, J. Spisak, S. Takakura, G. P. Teply, K. Yamada, and Polarbear Collaboration, *Phys. Rev. D* **110**, 063013 (2024), arXiv:2403.02096 [astro-ph.CO].

[26] X. Xue, S. Dai, H. Nhan Luu, T. Liu, J. Ren, J. Shu, Y. Zhao, A. Zic, N. D. R. Bhat, Z.-C. Chen, Y. Feng, G. Hobbs, A. Kapur, R. N. Manchester, R. Mandow, S. Mishra, D. J. Reardon, C. J. Russell, R. M. Shannon, S. Wang, L. Zhang, S. Zhang, and X. Zhu, arXiv e-prints , arXiv:2412.02229 (2024), arXiv:2412.02229 [astro-ph.HE].

[27] M. Benisty, C. Dominik, K. Follette, A. Garufi, C. Ginski, J. Hashimoto, M. Keppler, W. Kley, and J. Monnier, in *Protostars and Planets VII*, Astronomical Society of the Pacific Conference Series, Vol. 534, edited by S. Inutsuka, Y. Aikawa, T. Muto, K. Tomida, and M. Tamura (2023) p. 605, arXiv:2203.09991 [astro-ph.EP].

[28] S. Chigusa, T. Moroi, and K. Nakayama, *Physics Letters B* **803**, 135288 (2020), arXiv:1911.09850 [astro-ph.CO].

[29] T. Fujita, R. Tazaki, and K. Toma, *Phys. Rev. Lett.* **122**, 191101 (2019), arXiv:1811.03525 [astro-ph.CO].

[30] H. Nakatsuka, S. Morisaki, T. Fujita, J. Kume, Y. Michimura, K. Nagano, and I. Obata, *Phys. Rev. D* **108**, 092010 (2023), arXiv:2205.02960 [astro-ph.CO].

[31] J. I. Read, *Journal of Physics G Nuclear Physics* **41**, 063101 (2014), arXiv:1404.1938 [astro-ph.CO].

ph.GA].

- [32] J. Hashimoto, M. Tamura, T. Muto, T. Kudo, M. Fukagawa, T. Fukue, M. Goto, C. A. Grady, T. Henning, K. Hodapp, and et al., [ApJL 729, L17 \(2011\)](#), [arXiv:1102.4408 \[astro-ph.SR\]](#).
- [33] J. D. Monnier, T. J. Harries, J. Bae, B. R. Setterholm, A. Laws, A. Aarnio, F. C. Adams, S. Andrews, N. Calvet, C. Espaillat, L. Hartmann, S. Kraus, M. McClure, C. Miller, R. Oppenheimer, D. Wilner, and Z. Zhu, [Astrophys. J. 872, 122 \(2019\)](#), [arXiv:1901.02467 \[astro-ph.EP\]](#).
- [34] J. de Boer, M. Langlois, R. G. van Holstein, J. H. Girard, D. Mouillet, A. Vigan, K. Dohlen, F. Snik, C. U. Keller, C. Ginski, D. M. Stam, J. Milli, Z. Wahhaj, M. Kasper, H. M. Schmid, P. Rabou, L. Gluck, E. Hugot, D. Perret, P. Martinez, L. Weber, J. Pragt, J.-F. Sauvage, A. Boccaletti, H. Le Coroller, C. Dominik, T. Henning, E. Lagadec, F. Ménard, M. Turatto, S. Udry, G. Chauvin, M. Feldt, and J.-L. Beuzit, [A&A 633, A63 \(2020\)](#), [arXiv:1909.13107 \[astro-ph.IM\]](#).
- [35] Y. Doi, T. Hasegawa, R. S. Furuya, S. Coudé, C. L. H. Hull, D. Arzoumanian, P. Bastien, M. C.-Y. Chen, J. Di Francesco, R. Friesen, M. Houde, S.-i. Inutsuka, S. Mairs, M. Matsumura, T. Onaka, S. Sadavoy, Y. Shimajiri, M. Tahani, K. Tomisaka, C. Eswaraiah, P. M. Koch, K. Pattle, C. Won Lee, M. Tamura, D. Berry, T.-C. Ching, J. Hwang, W. Kwon, A. Soam, J.-W. Wang, S.-P. Lai, K. Qiu, D. Ward-Thompson, D.-Y. Byun, H.-R. V. Chen, W. P. Chen, Z. Chen, J. Cho, M. Choi, Y. Choi, A. Chrysostomou, E. J. Chung, P. N. Diep, H.-Y. Duan, L. Fanciullo, J. Fiege, E. Franzmann, P. Friberg, G. Fuller, T. Gledhill, S. F. Graves, J. S. Greaves, M. J. Griffin, Q. Gu, I. Han, J. Hatchell, S. S. Hayashi, T. Hoang, T. Inoue, K. Iwasaki, I.-G. Jeong, D. Johnstone, Y. Kanamori, J.-h. Kang, M. Kang, S.-j. Kang, A. Kataoka, K. S. Kawabata, F. Kemper, G. Kim, J. Kim, K.-T. Kim, K. H. Kim, M.-R. Kim, S. Kim, J. M. Kirk, M. I. N. Kobayashi, V. Konyves, T. Kusune, J. Kwon, K. Lacaille, C.-Y. Law, C.-F. Lee, H. Lee, J.-E. Lee, S.-S. Lee, Y.-H. Lee, D. Li, D. Li, H.-b. Li, H.-L. Liu, J. Liu, S.-Y. Liu, T. Liu, I. de Looze, A.-R. Lyo, B. C. Matthews, G. H. Moriarty-Schieven, T. Nagata, F. Nakamura, H. Nakanishi, N. Ohashi, G. Park, H. Parsons, N. Peretto, T.-S. Pyo, L. Qian, R. Rao, M. G. Rawlings, B. Retter, J. Richer, A. Rigby, H. Saito, G. Savini, A. M. M. Scaife, M. Seta, H. Shinnaga, Y.-W. Tang, Y. Tsukamoto, S. Viti, H. Wang, A. P. Whitworth, H.-W. Yen, H. Yoo, J. Yuan, H.-S. Yun, T. Zenko, C.-P. Zhang, G. Zhang, Y. Zhang, J. Zhou, L. Zhu, P. André, C. D. Dowell, S. P. S. Eyres, S. Falle, S. van Loo, and J.-F. Robitaille, [Astrophys. J. 899, 28 \(2020\)](#), [arXiv:2007.00176 \[astro-ph.GA\]](#).

- [36] K. V. Mardia and P. E. Jupp, *Directional Statistics* (Wiley, Chichester, 2000).
- [37] B. B. Ren, M. Benisty, C. Ginski, R. Tazaki, N. L. Wallack, J. Milli, A. Garufi, J. Bae, S. Facchini, F. Ménard, P. Pinilla, C. Swastik, R. Teague, and Z. Wahhaj, [Astronomy & Astrophysics](#) **680**, A114 (2023), arXiv:2310.08589 [astro-ph.EP].
- [38] Z. Wahhaj, J. Milli, C. Romero, L. Cieza, A. Zurlo, A. Vigan, E. Peña, G. Valdes, F. Cantalloube, J. Girard, and B. Pantoja, [A&A](#) **648**, A26 (2021), arXiv:2101.08268 [astro-ph.EP].
- [39] R. Bähre, B. Döbrich, J. Dreyling-Eschweiler, S. Ghazaryan, R. Hodajerdi, D. Horns, F. Januschek, E.-A. Knabbe, A. Lindner, D. Notz, A. Ringwald, J. E. von Seggern, R. Stromhagen, D. Trines, and B. Willke, [Journal of Instrumentation](#) **8** (9), T09001, arXiv:1302.5647 [physics.ins-det].
- [40] K. Y. L. Su, A. Gáspár, G. H. Rieke, R. Malhotra, L. Matrá, S. G. Wolff, J. M. Leisenring, C. Beichman, and M. Ygouf, [Astrophys. J.](#) **977**, 277 (2024), arXiv:2410.23636 [astro-ph.EP].